

# Correlation effects in (111) bilayers of perovskite transition-metal oxides

Satoshi Okamoto,<sup>1,\*</sup> Wenguang Zhu,<sup>2</sup> Yusuke Nomura,<sup>3</sup> Ryotaro Arita,<sup>3</sup> Di Xiao,<sup>4</sup> and Naoto Nagaosa<sup>3,5</sup>

<sup>1</sup>*Materials Science and Technology Division, Oak Ridge National Laboratory, Oak Ridge, Tennessee 37831, USA*

<sup>2</sup>*ICQD/HFNL, University of Science and Technology of China, Hefei, Anhui 230026, China*

<sup>3</sup>*Department of Applied Physics, the University of Tokyo, Hongo, Bunkyo-ku, Tokyo 113-8656, Japan*

<sup>4</sup>*Department of Physics, Carnegie Mellon University, Pittsburgh, Pennsylvania 15213, USA*

<sup>5</sup>*RIKEN Center for Emergent Matter Science (CEMS), Wako, Saitama 351-0198, Japan*

We investigate the correlation-induced Mott, magnetic and topological phase transitions in artificial (111) bilayers of perovskite transition-metal oxides  $\text{LaAuO}_3$  and  $\text{SrIrO}_3$  for which the previous density-functional theory calculations predicted topological insulating states. Using the dynamical-mean-field theory with realistic band structures and Coulomb interactions,  $\text{LaAuO}_3$  bilayer is shown to be far away from a Mott insulating regime, and a topological-insulating state is robust. On the other hand,  $\text{SrIrO}_3$  bilayer is on the verge of an orbital-selective topological Mott transition and turns to a trivial insulator by an antiferromagnetic ordering. Oxide bilayers thus provide a novel class of topological materials for which the interplay between the spin-orbit coupling and electron-electron interactions is a fundamental ingredient.

PACS numbers: 73.21.-b 73.43.-f, 71.27.+a

## I. INTRODUCTION

Topological insulators (TIs) are novel quantum states of matter characterized by the nontrivial band topology due to the relativistic spin-orbit coupling (SOC) [1–7]. While the TI states are essentially single-particle phenomena, the interplay between the SOC and strong Coulomb interactions in electronic systems has gained considerable attention [8–10]. A variety of effects between these two couplings has been theoretically explored, such as TI states induced by Coulomb interactions [11, 12], competition and/or cooperation between the two in a Kane-Mele-Hubbard (KMH) model [13–15] or a Bernevig-Hughes-Zhang (BHZ) model [16–18], and topological Kondo insulators [19–21].

Recently, based on the tight-binding modeling and subsequent density-functional theory (DFT) calculations, bilayers of perovskite transition-metal oxides (TMOs)  $\text{ABO}_3$  grown along the [111] crystallographic axis, i.e., (111) bilayers, were proposed as possible candidates for two-dimensional TIs [22]. In such (111) bilayers, buckled honeycomb lattice is formed by B-site transition-metal ions (Fig. 1). TMOs are known to cover a vast extension of unconventional phenomena due to the strong electron-electron and electron-lattice interactions [23]. Because of the active orbital degrees of freedom, the interplay between the SOC and correlation effects could induce phenomena that are absent in abstract theoretical models or those for semiconductors, such as a spin-orbit Mott insulator [24]. Furthermore, the recent development in synthesizing artificial TMO heterostructures provides great tunability over fundamental physical parameters [25]. Once realized in TMOs, combining TIs with other novel states would allow us to study further novel phenomena utilizing proximity effects involving TIs [26, 27]. However, while single-electron properties are treated rather

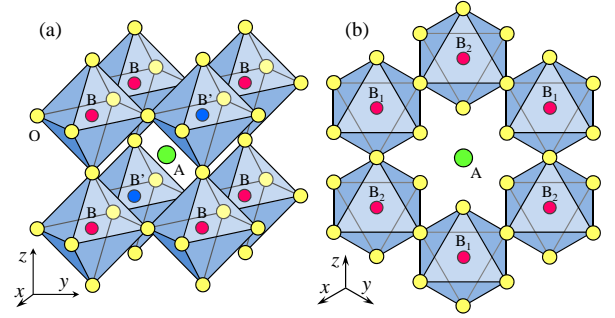


FIG. 1: (Color online) Buckled honeycomb lattice formed in (111) bilayer of perovskite TMO  $\text{ABO}_3$ . (a) (111) bilayer of  $\text{ABO}_3$  sandwiched by insulating  $\text{AB}'\text{O}_3$ . (b)  $\text{ABO}_3$  forms buckled honeycomb lattice with two sublattices  $B_1$  and  $B_2$ .

accurately using DFT [22, 28], including the SOC, the effect of electron-electron interactions has not been addressed except for limiting cases for such TMO bilayers [22, 29–35].

In this paper, we provide concrete examples of the interplay between the SOC and correlation effects in (111) TMO bilayers. As specific examples, we consider  $\text{SrIrO}_3$  (SIO) and  $\text{LaAuO}_3$  (LAO), for which the previous DFT calculations predicted TI states [22], and investigate the correlation-induced phase transitions by means of the dynamical-mean-field theory (DMFT) [36]. It is shown that LAO bilayer is far from Mott insulating and antiferromagnetic (AF) insulating regimes, and a TI state is robust. On the contrary, the correlation effect is significant for SIO bilayer, and an AF trivial insulating state is realized. This is induced by a relatively narrow bandwidth of near-Fermi-level states with the dominant  $J_{\text{eff}} = 1/2$  character, which undergoes an orbital-selective topological Mott transition when the magnetic ordering is suppressed. Our results indicate that the interplay between

the SOC and correlations is diverse, showing the strong material dependence, and provide further guidelines for studying topological phenomena in TMOs in both bulk and artificial heterostructures.

The rest of the paper is organized as follows. In Sec. II, the methodology is described, and in Sec. III numerical results are presented. Section IV is devoted to the summary.

## II. METHOD

For a realistic treatment on the band effects, we generate Wannier functions [37] from the outputs of DFT calculations. The DFT calculations are performed using *Vienna Ab initio Simulation Package* (VASP [38]) with the use of the projector augmented wave method [39] with the generalized gradient approximation in the parametrization of Perdew, Burke and Enzerhof [40] for exchange correlation. In this work, to obtain the Wannier functions, thinner supercells are adopted than in Ref. [22], consisting of 6  $\text{AO}_3$  and 6 B layers along the [111] direction with (A,B) = (Sr,Ti) or (La,Al) with two adjacent B layers replaced by TM ions. As in the previous study, we fix the in-plane lattice parameter to that of bulk  $\text{SrTiO}_3$  or  $\text{LaAlO}_3$  and optimize the out-of-plane lattice parameter as well as the atomic position using a  $6 \times 6 \times 1$  k-point mesh including the  $\Gamma$  point (0,0,0) for integration over the Brillouin zone. The SOC is included after the lattice optimization using the default method in VASP. We have checked that current DFT results agree with the previous ones.

Figure 2 shows the resultant DFT dispersion relations [(blue) solid lines] and those of Wannier functions. With the finite SOC,  $\text{SrIrO}_3$  (111) bilayer was found to have tiny but finite magnetic moments, which prevent us from constructing maximally localized Wannier functions (MLWFs) with proper symmetries, whose dispersion relations are given by (red) dashed lines [Fig. 2 (a), Wannier1]. To completely suppress the magnetism, we turned off the SOC and derived MLWFs and an effective tight-binding model. Then, the following atomic SOC is added to such a model Hamiltonian

$$H_{\text{SOC}} = \frac{\lambda}{2} \sum_{\vec{r}\sigma\sigma'} \sum_{\tau\tau'\tau''} i\varepsilon_{\tau\tau'\tau''} d_{\vec{r}\tau\sigma} \sigma_{\sigma\sigma'}^{\tau''} d_{\vec{r}\tau'\sigma'}, \quad (1)$$

where the following convention for the orbital index is used:  $|a\rangle = |d_{yz}\rangle$ ,  $|b\rangle = |d_{zx}\rangle$ , and  $|c\rangle = |d_{xy}\rangle$ .  $\sigma^\tau$  with  $\tau = a, b, c$  is the Pauli matrix, and  $\varepsilon_{\tau\tau'\tau''}$  is the Levi-Civita antisymmetric tensor. Using  $\lambda$  as a fitting parameter, we derive the model Hamiltonian for  $\text{SrIrO}_3$  (111) bilayer. By matching the band gap, we optimized  $\lambda$  as 0.36 eV. The resulting dispersion relations are given by (green) dash-dot lines [Fig. 2 (a), Wannier2]. The data set Wannier2 is used in our realistic DMFT calculation for  $\text{SrIrO}_3$  (111) bilayer. While we did not have issues

associated with magnetic moments for  $\text{LaAuO}_3$  (111) bilayer, we found that the symmetry of Wannier functions is progressively reduced by iterations. To avoid this, we set the number of iterations to zero, and derived “one-shot” Wannier functions including the SOC. The resultant dispersion relations are given by (red) dashed lines [Fig. 2 (b), Wannier]. This data set is used in our realistic DMFT calculation for  $\text{LaAuO}_3$  (111) bilayer.

The dispersion relations for 40-site thick zigzag slab of  $\text{SrIrO}_3$  (111) bilayer using the Wannier2 parameter set are given in Fig. 2 (c). Corresponding results for 40-site thick zigzag slab of  $\text{LaAuO}_3$  (111) bilayer are given in Fig. 2 (d). Slab dispersions confirm that both  $\text{SrIrO}_3$  (111) bilayer and  $\text{LaAuO}_3$  (111) bilayer are topological insulators with gapless edge modes crossing the Fermi level indicated by light (red) lines.

To examine magnetic ordering, we use structures obtained for paramagnetic phases within DFT as explained above. Additionally, we performed DFT+ $U$  calculations using the same structures.

Correlation effects are dealt with using DMFT with the exact diagonalization (ED) impurity solver [41–43]. Here, the effective medium is approximated as a finite number of bath sites coupled to eigenstates of the local non-interacting Hamiltonian [42]. With the SOC and the trigonal crystal field, all degeneracies in  $d$  multiplet are lifted except for the Kramers degeneracy [22]. For a  $t_{2g}$  system SIO there are three Kramers doublets, and for an  $e_g$  system LAO there are two Kramers doublets. Thus, we introduce two bath sites per Kramers doublet for SIO and three bath sites per doublet for LAO [44]. Note that the highest energy doublet for SIO bilayer has the strong  $J_{eff} = 1/2$  character, while the other two doublets have the  $J_{eff} = 3/2$  characters. As the typical gap amplitude of our systems is  $\sim 0.01$ -0.1 eV, we introduce temperature  $T = 0.01$  eV and retain the lowest eigenstates of the interacting impurity Hamiltonians with Boltzmann factors larger than  $10^{-5}$ . The DMFT self-consistency condition is closed by updating the bath Green’s functions at each iteration by minimizing with a conjugate gradient algorithm a distance function that includes frequency dependence on the discrete Matsubara frequency  $\omega_n = (2n+1)\pi T$  with a frequency weighting  $1/|\omega_n|$  [45]. The further details of the DMFT including the self-consistency scheme are presented in the Appendix.

## III. RESULTS

We begin with the typical paramagnetic (PM) bulk spectral functions for (a) SIO bilayer and (b) LAO bilayer with  $U = 2.0$  and  $J = 0.2$  eV as shown in Fig. 3. Here,  $U$  is the intraorbital Coulomb interaction and  $J$  is the interorbital exchange and pair transfer. The interorbital Coulomb interaction is taken to be  $U' = U - 2J$

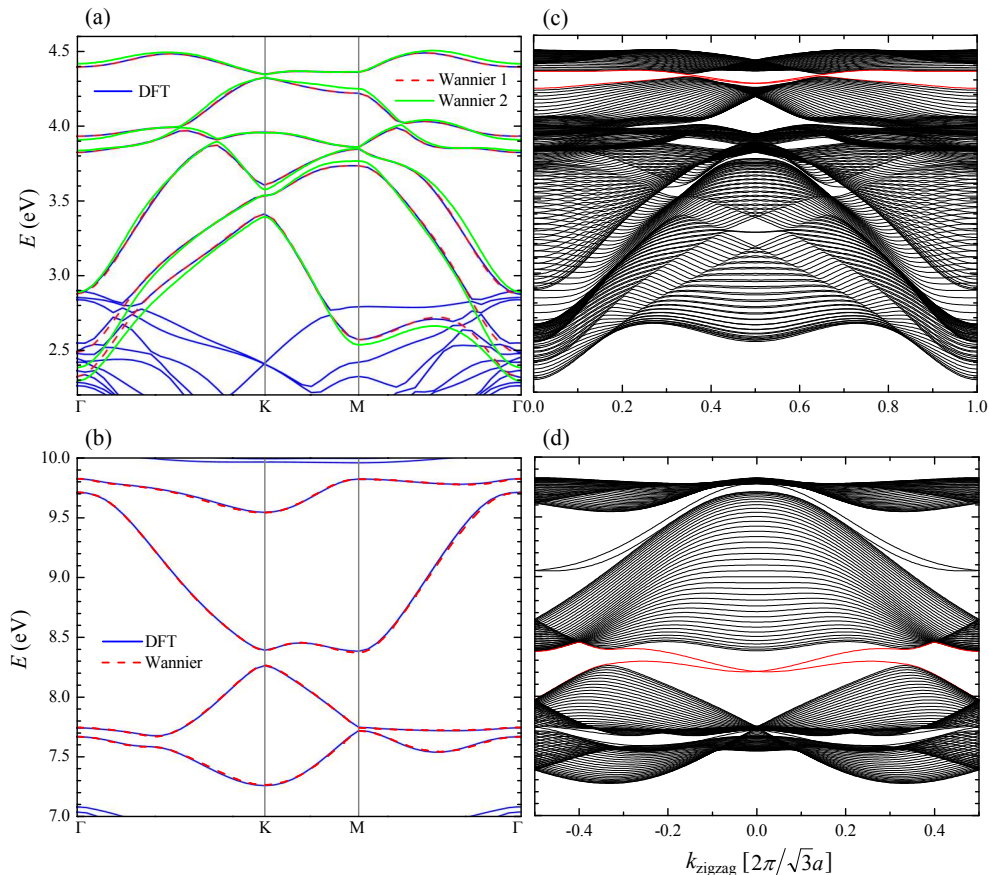


FIG. 2: (Color online) Bulk dispersion relations (a), (b) and dispersion relations for 80-site thick zigzag slabs (c), (d) of our (111) bilayers. (a), (c) SrIrO<sub>3</sub> (111) bilayer with the Fermi level located at  $E = 4.335$  eV. (b), (d) LaAuO<sub>3</sub> (111) bilayer with the Fermi level at 8.31 eV.  $a$  is the nearest neighbor bond length projected on the (111) plane.

throughout the paper. The spectral functions are computed using the self-energy directly obtained on the real axis, where the  $\delta$  function is broadened by using the logarithmic Gaussian function [46]. While both systems have similar bare band width  $\sim 2$  eV, the effect of correlations is notably different. For SIO bilayer, two nearly-flat dispersions appear at the Fermi level  $\omega = 0$ . These bands are mainly coming from the  $J_{eff} = 1/2$  states, but their effective mass is enhanced significantly due to the correlation effects and a large amount of spectral weight is transferred to higher energy regimes, forming the upper Hubbard band at  $\sim 1$  eV and the lower Hubbard band at  $\sim -0.3$  eV. The other states mainly from  $J_{eff} = 3/2$  states are relatively unaffected, and their dispersion relations are nearly identical to those of non-interacting model with about 0.5 eV downshift and broadening due to the imaginary part of the self-energy. On the other hand, the spectral function for LAO bilayer is not modified from the non-interacting case except for the moderate band renormalization and broadening away from the Fermi level.

### A. Mott transition

In order to see the nature of correlation-induced Mott transition, we plot the quasiparticle weight and the gap amplitude of two systems as a function of  $U$  in Fig. 4. The quasiparticle weight of Kramers doublet  $\alpha$  is evaluated from the self-energy at the lowest Matsubara frequency as  $Z_\alpha = [1 - \Im \Sigma_\alpha(i\omega_0)/\omega_0]^{-1}$ . To avoid the broadening of the spectral function by the imaginary part of the self-energy, the gap amplitude is evaluated from quasiparticle dispersions [47]. In both cases, the gap amplitude is monotonically decreased with increasing  $U$  and does not show a transition to a high  $U$  TI state in which the insulating gap increases with  $U$  as reported for SIO bilayer in Ref. [28]. On the contrary, the gap amplitude is strongly correlated with the (smallest) quasiparticle weight, and they become zero simultaneously at Mott transitions. For SIO bilayer, one of three Kramers doublets with the  $J_{eff} = 1/2$  character undergoes the Mott transition (filled squares) while the other two with the  $J_{eff} = 3/2$  character do not (filled and open circles). This situation resembles that in the single-layer perovskite Sr<sub>2</sub>IrO<sub>4</sub> [48]. But, the transition

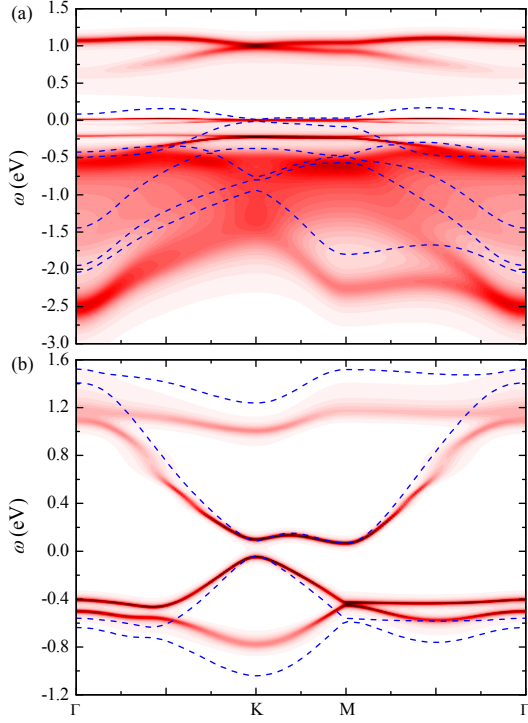


FIG. 3: (Color online) Bulk spectral function for (a) SrIrO<sub>3</sub> bilayer and (b) LaAuO<sub>3</sub> bilayer with  $U = 2.0$  and  $J = 0.2$  eV. Dotted lines show dispersion relations of non-interacting models.

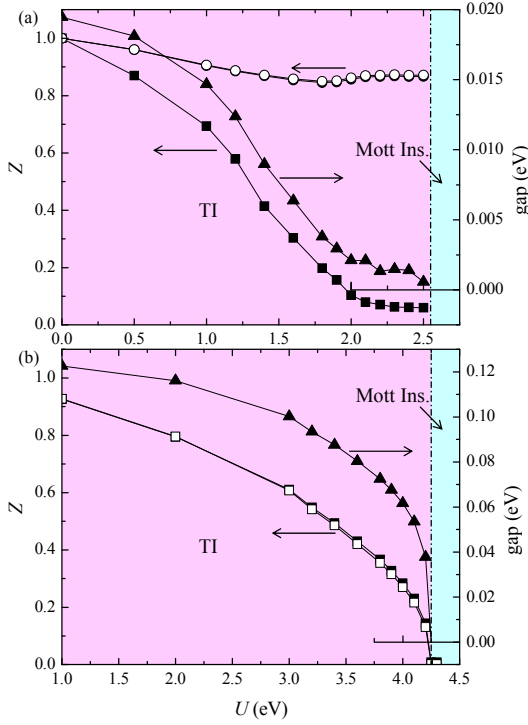


FIG. 4: (Color online) Quasiparticle weight  $Z$  and gap amplitude for (a) SrIrO<sub>3</sub> bilayer and (b) LaAuO<sub>3</sub> bilayer as a function of  $U$  with  $J/U = 0.1$ .

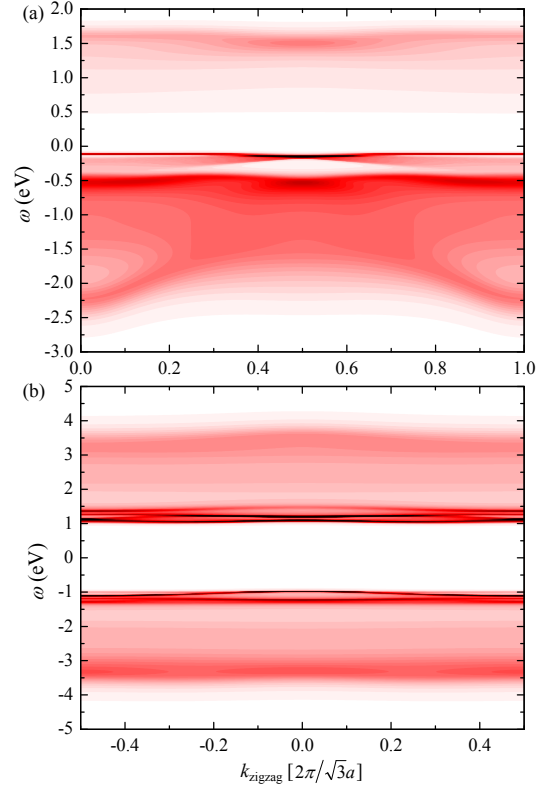


FIG. 5: (Color online) Edge spectral functions for 40-site thick zigzag slabs of (a) SrIrO<sub>3</sub> (111) bilayer with  $U = 2.6$  eV and  $J = 0.26$  eV and (b) LaAuO<sub>3</sub> bilayer with  $U = 4.4$  eV and  $J = 0.44$  eV without a magnetic ordering. These are in Mott insulating phases.

in SIO bilayer accompanies the change in the band topology from a nontrivial one to a trivial one as confirmed from the fully gapped edge spectra in the latter as discussed later. Thus, this transition is an orbital-selective topological Mott transition. For LAO bilayer, the quasi-particle weights of two Kramers doublets (filled and open squares) show nearly-identical  $U$  dependence. Whether or not PM Mott insulating states of two systems support gapless “spinon” edge states, i.e. topological Mott insulators [9], is a very interesting question but remains beyond the scope of the current single-site DMFT.

Figure 5 shows the edge spectral functions for 40-site thick zigzag slabs of (a) SrIrO<sub>3</sub> bilayer with  $U = 2.6$  eV and  $J = 0.26$  eV and (b) LaAuO<sub>3</sub> bilayer with  $U = 4.4$  eV and  $J = 0.44$  eV without a magnetic ordering. As seen in Fig. 4, these are in Mott insulating regimes. The absence of edge modes crossing the Fermi level at  $\omega = 0$  indicates both are in trivial phases at least “electronically.” There is a possibility that the nontrivial band topology remains in spinon dispersions supporting bulk band gaps and gapless edge modes, i.e., topological Mott insulators, but the current DMFT does not have access to such states.

## B. Magnetic ordering

We next study the effect of magnetic ordering. From both a weak-coupling approach and a strong-coupling approach [32], a Néel AF ordering is expected in SIO bilayer. Our DFT calculation indeed found the Néel AF ordering with magnetic moments primarily lying along the [111] axis. While the similar ordering is expected in LAO bilayer, our DFT calculations with  $U$  up to 4 eV and  $J/U$  up to  $\sim 0.2$  did not find any magnetic ordering. This could be ascribed to the fact that the local moment formation is underestimated in DFT. Nevertheless, we assume the Néel AF ordering for both systems by taking the [111] axis, perpendicular to the plane, as the spin quantization axis and examine its stability.

Figure 6 shows the magnetic order parameters and the gap amplitude for (a) SIO and (b) LAO. As expected from the smaller critical  $U$  for the Mott transition in SIO, the critical  $U$  for an AF ordering is also small,  $U \sim 0.5$  eV. In Fig. 6 (a), we also plot the magnetic order parameters obtained by generalized gradient approximation (GGA)+ $U$ . The critical  $U$  for the AF ordering appears to be slightly smaller than the present DMFT result and much smaller than local density approximation + $U$  results in Ref. [28] where the AF ordering appears at  $U > 3$  eV. In both the DMFT and GGA+ $U$  results, the orbital moment  $\mu_L$  and the spin moment  $\mu_S$  are tilted with each other. In GGA+ $U$ ,  $\mu_S$  is deviated from the [111] direction more strongly than  $\mu_L$ . In DMFT, both  $\mu_{L,S}$  turned out to be tilted by a similar amount.  $|\mu_L|/|\mu_S|$  is found to be  $\sim 1.7$  (smaller than 2). This indicates the deviation of the spin symmetry from the  $SU(2)$  point due to the local trigonal field by which the SOC active doublet  $e'_g$  is lower than the singlet  $a_{1g}$ . On the contrary,  $|\mu_L|/|\mu_S|$  becomes larger than 2 at  $U > 2$  eV by GGA+ $U$ . In addition,  $|\mu_L|$  and  $|\mu_S|$  are found to be larger in DMFT than in GGA+ $U$ . These differences are presumably from the better description by DMFT for the local moment formation, which becomes important even at small  $U$  [see Fig. 4 (a)]. In contrast to GGA+ $U$ , our DMFT calculation did find the stable AF ordering in LAO at  $U \gtrsim 2.1$  eV. As a  $\text{Au}^{+3}$  ion has the  $e_g^2$  electron configuration, DFT+ $U$  requires very large  $J$  to induce local moments  $S = 1$ . On the other hand, with finite  $J$ ,  $e_g^2$  states with  $S = 1$  always have larger weights than those with  $S = 0$ . These weights increase with increasing  $J$ , and therefore a magnetic ordering can be induced more easily in DMFT.

In SIO bilayer, an AF Néel ordering was found to destroy the TI state immediately. This is because, in a honeycomb lattice with the AF ordering, there is no combined symmetry with the time reversal by which the system remains invariant [49]. In LAO bilayer on the other hand, there appears a finite window for an AF TI where the gapless edge states and bulk magnetic ordering (time-reversal symmetry breaking) coexist as discussed

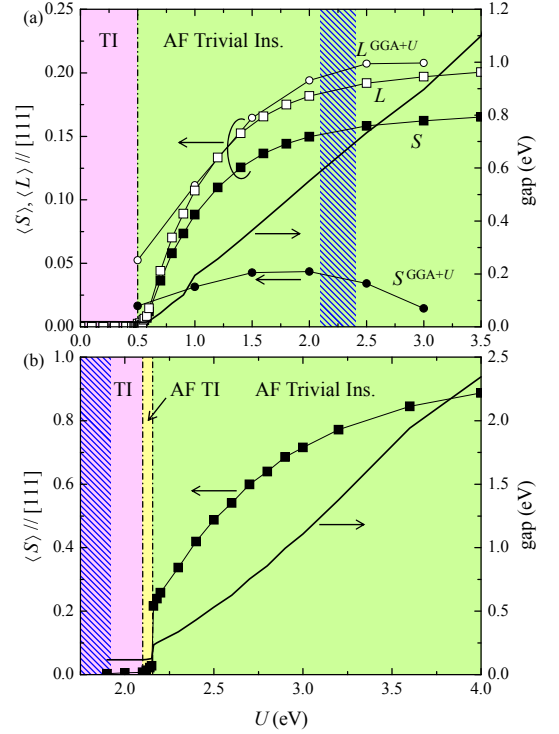


FIG. 6: (Color online) Staggered spin ( $S$ ) and angular momentum ( $L$ ) and gap amplitude for (a)  $\text{SrIrO}_3$  bilayer and (b)  $\text{LaAuO}_3$  bilayer with antiferromagnetic ordering as a function of  $U$  with  $J/U = 0.1$ . In (a), results of GGA+ $U$  are also plotted for spin  $S^{\text{GGA}+U}$  and angular momentum  $L^{\text{GGA}+U}$ . Shaded areas are realistic parameter regimes estimated by cRPA.

later. This comes from the fact that the spin component perpendicular to the [111] plane is conserved in our  $e_g$  electron model [22], and therefore LAO bilayer consists of two copies of Chern insulators with the opposite Chern number. The transition between the AF TI phase and the AF trivial insulating phase in LAO bilayer is found to be of the first order accompanied by a jump in the staggered magnetic moment. Thus, the gap closing is avoided. This transition could become a continuous one by including spatial correlations beyond the single-site DMFT. For instance, for a correlated BHZ model, a single-site DMFT calculation found a discontinuous transition from a PM TI phase to an AF trivial phase [16]. But a variational cluster approach found a continuous transition accompanied by the gap closing, leaving a finite window for an AF TI phase [17].

Here, we examine the nature of antiferromagnetic phases in  $\text{LaAuO}_3$  bilayer in more detail. Figure 7 shows the edge spectral functions for 40-site thick zigzag slabs of antiferromagnetic  $\text{LaAuO}_3$  (111) bilayer with (a)  $U = 2.14$  eV and (b)  $U = 2.16$  eV with  $J/U = 0.1$ . Because of the Néel antiferromagnetic ordering, the symmetry between  $k > 0$  and  $k < 0$  is broken. While the antiferromagnetic ordering breaks the time-reversal sym-



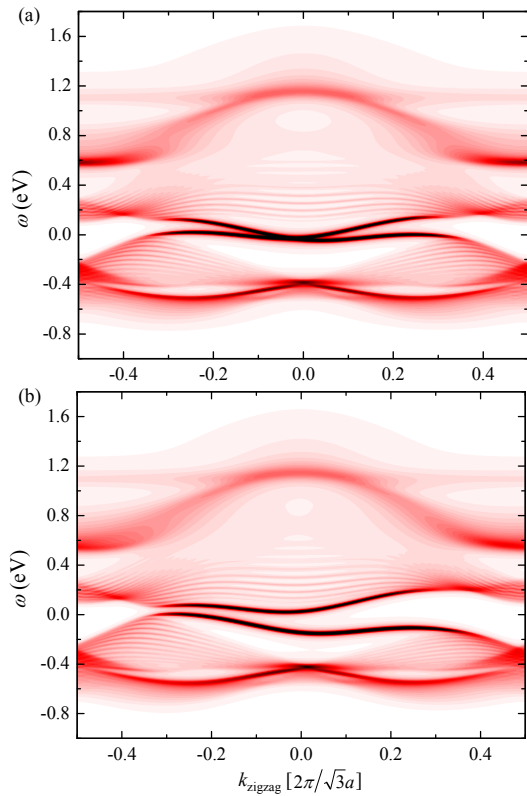


FIG. 7: (Color online) Edge spectral functions for 40-site thick zigzag slabs of LaAuO<sub>3</sub> (111) bilayer with (a)  $U = 2.14$  eV and (b)  $U = 2.16$  eV with  $J/U = 0.1$ . There are gapless edge modes at the Fermi level  $\omega = 0$  in (a), while there are none in (b).

metry, the combined symmetry between the time reversal and mirror (mirror plane perpendicular to the zigzag direction) remains. As a result, each mode is twofold degenerate. We see gapless edge modes at the Fermi level in (a) while not in (b), indicating the former is in a topologically nontrivial phase but the latter is in a trivial phase.

### C. Realistic parameter regimes

Are SIO and LAO in AF trivial insulating phases or TI phases? If they are in AF trivial phases, can we turn them into TI phases by suppressing magnetic ordering? To answer these questions, we estimate realistic Coulomb interactions by using the constrained random phase approximation (cRPA)[50–54]. For SIO bilayer, we took the Slater parameters  $F_{0,2,4}$  for Sr<sub>2</sub>IrO<sub>4</sub> from Ref. [48] and deduced  $U$  and  $J$  as 2.232 eV and 0.202 eV, respectively, for the  $\{xy, yz, zx\}$  basis.

For LAO bilayer, we directly computed these parameters for the  $\{3z^2 - r^2, x^2 - y^2\}$  basis. For this purpose, we first constructed a thinner supercell consisting of two LaAuO<sub>3</sub> and one LaAlO<sub>3</sub> layers along the [111] direction in which the local structure taken from the previous re-

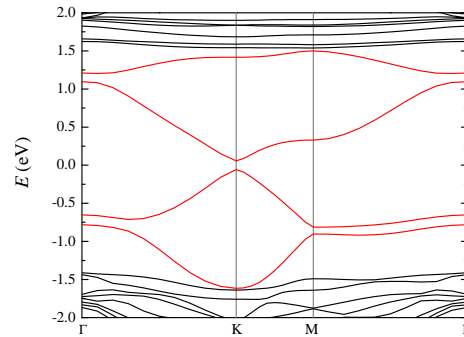


FIG. 8: (Color online) Bulk dispersion relation for [LaAuO<sub>3</sub>]<sub>2</sub>[LaAlO<sub>3</sub>]<sub>1</sub> superlattice, which is used to estimate the Coulomb interaction by cRPA. Au 5d bands are indicated by light (red) lines. The Fermi level is located at  $E = 0$  eV.

sults with thicker LaAlO<sub>3</sub> layers. The dispersion relation for the thinner supercell is presented in Fig. 8. We notice that the overall feature is well captured. While the Au 5d bands are slightly wider than those in Fig. 2 (b), these are separated from other bands. Thus the realistic  $U$  for thicker LAO bilayer might be slightly larger than this supercell, but not significantly. We then used the density response code for Elk (Ref. [51]). The polarization function was expanded in plane waves with an energy cutoff of 5 Ry and the number of empty bands considered in the polarization calculation was set to 80. We performed the calculation with  $4 \times 4 \times 2$   $\mathbf{k}$  mesh and  $3 \times 3 \times 1$   $\mathbf{k}$  mesh, and we found the difference in the Coulomb interaction parameters is within 5 %. Resultant  $U$  and  $J$  are  $U = 1.80$  eV and  $J = 0.225$  eV, respectively. Note that  $J/U \approx 0.1$  in both SIO and LAO. These realistic parameter regimes are approximately indicated by shades in Fig. 6.

With the realistic parameters, we confirmed that an AF Néel ordered state is realized in SIO bilayer and a PM state in LAO bilayer. From the edge spectra, the AF SIO is an AF trivial insulator while the PM LAO is a TI (see Fig. 9). Note that the critical  $U$  for a PM-AF transition is supposed to be underestimated by the current DMFT because the long-wave length quantum fluctuation is absent. Thus LAO is further away from AF phases. When an AF Néel order is suppressed, SIO bilayer turns into a PM TI not a PM Mott insulator. This situation is quite similar to that in Sr<sub>2</sub>IrO<sub>4</sub> [48, 55]. Since the gap amplitude of PM SIO bilayer is about 0.002 eV, which is an order of magnitude smaller than temperature  $T = 0.01$  eV [see Fig. 4 (a)], thermal broadening might hinder the TI nature and SIO bilayer would behave as a topological semimetal. In reality, finite spatial correlations may induce a pseudogap even without an AF long-range order in a PM phase of SIO bilayer. Whether or not such a pseudogap phase supports gapless electron or spinon edge modes remains a very interesting problem. Even if a pseudogap is created, a high pressure may push SIO bilayer back to a TI. Also, carrier doping may induce the

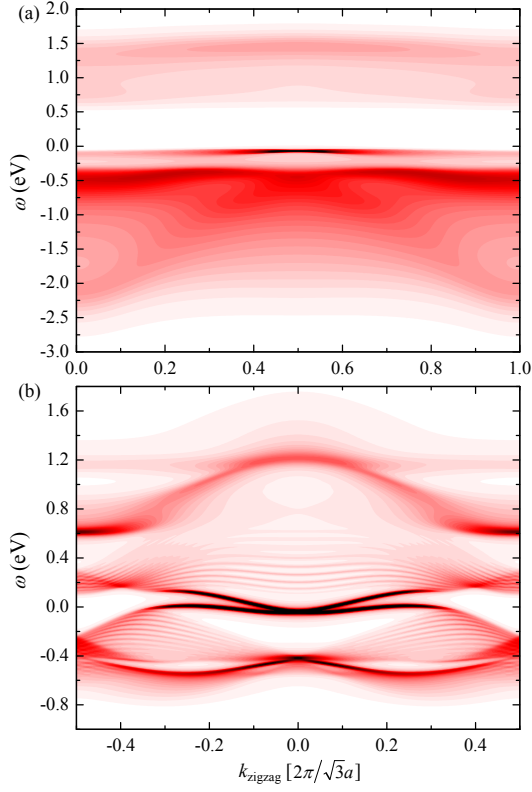


FIG. 9: (Color online) Edge spectral functions for 40-site thick zigzag slabs of (a) SrIrO<sub>3</sub> bilayer with  $U = 2.232$  eV and  $J = 0.202$  eV and (b) LaAuO<sub>3</sub> bilayer with  $U = 1.80$  eV and  $J = 0.225$  eV.  $a$  is the nearest-neighbor distance projected on the [111] plane. Because of an AF ordering, SrIrO<sub>3</sub> bilayer does not support gapless edge modes.

unconventional superconductivity in SIO bilayer [32, 56].

#### IV. SUMMARY

To summarize, the electronic properties of (111) TMO bilayers are governed by the close interplay between the SOC and correlation effects. Using the realistic DMFT, the SOC is found to dominate in LAO bilayer, resulting in a moderately correlated TI. On the contrary, correlation effects overcome the SOC in SIO bilayer, driving it towards an orbital-selective topological Mott transition, where only one band with the strong  $J_{eff} = 1/2$  character undergoes “band insulator”–Mott insulator transition. SIO bilayer is further unstable against a Néel AF ordering, resulting in an AF trivial insulator. In contrast to a topological Kondo system where the nontrivial band topology comes from the hybridization between  $f$  states and the conduction band [57–59], the correlation effects in TMOs are Mott-Hubbard type and  $d$  states themselves hold the nontrivial band topology. The interplay between the SOC and correlation effects in artificial (111) TMO bilayers is thus diverse and brings about rich competing

phenomena, rendering unique playgrounds for studying such an interplay.

#### ACKNOWLEDGMENTS

S.O. thanks M. S. Bahramy, B.-J. Yang and J. Matsuno for their fruitful discussions and RIKEN CEMS for hospitality during his visit under the FIRST Theory Forum Visiting Scientist program. The research by S.O. is supported by the U.S. Department of Energy, Basic Energy Sciences, Materials Sciences and Engineering Division. W.Z. is supported by National Natural Science Foundation of China (No. 11374273). Y.N. is supported by Grant-in-Aid for JSPS Fellows (12J08652). D.X. is supported by AFOSR Grant No. FA9550-12-1-0479. N.N. is supported by Grant-in-Aids for Scientific Research (S) (No. 24224009) from the Ministry of Education, Culture, Sports, Science and Technology (MEXT) of Japan, Strategic International Cooperative Program (Joint Research Type) from Japan Science and Technology Agency, and by Funding Program for World-Leading Innovative R&D on Science and Technology (FIRST Program).

#### APPENDIX: DMFT SCHEME

The DMFT calculations are performed using a single-particle Hamiltonian consisting of the local part  $H_{local}$  and the nonlocal or band part  $H_{nonlocal}$  as parametrized in the Wannier basis and a many-body part  $H_U$ . Here, we express  $H_U$  in terms of real orbitals, either  $t_{2g}$  or  $e_g$ , as[60]

$$\begin{aligned}
 H_U = & U \sum_{\alpha} d_{\alpha\uparrow}^{\dagger} d_{\alpha\uparrow} d_{\alpha\downarrow}^{\dagger} d_{\alpha\downarrow} + U' \sum_{\alpha \neq \beta} d_{\alpha\uparrow}^{\dagger} d_{\alpha\uparrow} d_{\beta\downarrow}^{\dagger} d_{\beta\downarrow} \\
 & + (U' - J) \sum_{\alpha > \beta, \sigma} d_{\alpha\sigma}^{\dagger} d_{\alpha\sigma} d_{\beta\sigma}^{\dagger} d_{\beta\sigma} \\
 & + J \sum_{\alpha \neq \beta} \left( d_{\alpha\uparrow}^{\dagger} d_{\beta\uparrow} d_{\beta\downarrow}^{\dagger} d_{\alpha\downarrow} + d_{\alpha\uparrow}^{\dagger} d_{\beta\uparrow} d_{\alpha\downarrow}^{\dagger} d_{\beta\downarrow} \right), \quad (A1)
 \end{aligned}$$

where  $\alpha$  and  $\beta$  stand for  $(yz, zx, xy)$  for SIO and  $(3z^2 - r^2, x^2 - y^2)$  for LAO.  $U$  and  $U'$  are the intraorbital Coulomb interaction and the interorbital Coulomb interaction, respectively, and  $J$  represents the interorbital exchange interaction (fourth term) and the interorbital pair hopping (fifth term). For orbitals with the  $t_{2g}$  or  $e_g$  symmetry,  $U' = U - 2J$ . We then move on to the basis which diagonalizes the local non-interacting Hamiltonian  $H_{local}$  including the crystal field and the SOC, say  $d_{\xi\tau} = \sum_{\alpha\sigma} W_{\alpha\sigma, \xi\tau}^* d_{\alpha\sigma}$  with the eigenvalue  $\varepsilon_{\xi\tau}$ .  $\tau = \pm$  specifies a pair of Kramers doublet  $\xi$ . In the current ED-DMFT, the effective medium is approximated as a finite number of bath sites coupled to each Kramers doublet.

Thus, the impurity model to be diagonalized is written as

$$H_{imp} = H_{local} + H_U + \sum_{\xi\tau} \sum_{l=1}^{n_s} \times \left[ \varepsilon_{\xi\tau l} c_{\xi\tau l}^\dagger c_{\xi\tau l} + (V_{\xi\tau l} c_{\xi\tau l}^\dagger d_{\xi\tau} + h.c.) \right], \quad (A2)$$

where  $n_s$  is taken to be 2 for the  $t_{2g}$  system SIO and 3 for the  $e_g$  system LAO.

By solving  $H_{imp}$ , one obtains the interacting Green's function  $G_{\xi\tau}(i\omega_n)$  and the self-energy  $\Sigma_{\xi\tau}(i\omega_n) = \mathcal{G}_{\xi\tau}^{-1}(i\omega_n) - G_{\xi\tau}^{-1}(i\omega_n)$ , where the non-interacting Green's function is given by

$$\mathcal{G}_{\xi\tau}^{-1}(i\omega_n) = i\omega - \varepsilon_{\xi\tau} - \sum_l \frac{|V_{\xi\tau l}|^2}{i\omega_n - \varepsilon_{\xi\tau l}}. \quad (A3)$$

Parameters  $\varepsilon_{\xi\tau l}$  and  $V_{\xi\tau l}$  are fixed at each DMFT iteration by minimizing with a conjugate gradient algorithm a distance function

$$\Delta = \sum_{\xi\tau} \sum_n \left| \mathcal{G}_{\xi\tau}(i\omega) - g_{\xi\tau}^0(i\omega_n) \right|^2 \frac{1}{|\omega_n|}. \quad (A4)$$

Here,  $g_{\xi\tau}^0(i\omega_n)$  is the lattice non-interacting Green's function, which is obtained by

$$g_{\xi\tau}^0(i\omega_n) = \left[ g_{\xi\tau}^{-1}(i\omega_n) + \Sigma_{\xi\tau}(i\omega_n) \right]^{-1}, \quad (A5)$$

with the lattice interacting Green's function

$$g_{\xi\tau}(i\omega_n) = \sum_{\alpha\beta\sigma\sigma'} W_{\alpha\sigma,\xi\tau}^* g_{\alpha\sigma,\beta\sigma'}(i\omega_n) W_{\beta\sigma',\xi\tau}. \quad (A6)$$

Now, reviving the sublattice index  $\iota = 1, 2$ ,  $g_{\alpha\sigma,\beta\sigma'}^{(\iota)}(i\omega_n)$  is formally given by

$$g_{\alpha\sigma,\beta\sigma'}^{(\iota)}(i\omega_n) = \int \left( \frac{dk}{2\pi} \right)^2 \left[ \frac{1}{i\omega_n - \hat{H}_{local} - \hat{H}_{nonlocal}(\vec{k}) - \hat{\Sigma}(i\omega_n)} \right]_{\iota\alpha\sigma,\iota\beta\sigma'}. \quad (A7)$$

Here, the lattice self-energy matrix is expressed as

$$\hat{\Sigma}(i\omega_n) = \begin{bmatrix} \hat{\Sigma}^{(1)}(i\omega_n) & \\ & \hat{\Sigma}^{(2)}(i\omega_n) \end{bmatrix}, \quad (A8)$$

with  $\hat{\Sigma}^{(\iota)}(i\omega_n)$  given by

$$\Sigma_{\alpha\sigma,\beta\sigma'}^{(\iota)}(i\omega_n) = W_{\alpha\sigma,\xi\tau} \Sigma_{\xi\tau}^{(\iota)} W_{\beta\sigma',\xi\tau}^*. \quad (A9)$$

By symmetry,  $\Sigma_{\xi\tau}^{(\iota)}(i\omega_n) = \Sigma_{\xi}(i\omega_n)$  in a PM phase and  $\Sigma_{\xi\tau}^{(1)}(i\omega_n) = \Sigma_{\xi-\tau}^{(2)}(i\omega_n)$  in an AF phase.

---

\* okapon@ornl.gov

- [1] C. L. Kane and E. J. Mele, Phys. Rev. Lett. **95**, 146802 (2005).
- [2] A. B. Bernevig, T. L. Hughes, and S.-C. Zhang, Science **314**, 1757 (2006).
- [3] J. E. Moore and L. Balents, Phys. Rev. B **75**, 121306 (2007).
- [4] L. Fu, C. L. Kane, and E. J. Mele, Phys. Rev. Lett. **98**, 106803 (2007).
- [5] M. König, S. Wiedmann, C. Brüne, A. Roth, H. Buhmann, L. W. Molenkamp, X.-L. Qi, and S.-C. Zhang, Science **318**, 766 (2007).
- [6] D. Hsieh, D. Qian, L. Wray, Y. Xia, Y. S. Hor, R. J. Cava, and M. Z. Hasan, Nature (London) **452**, 970 (2008).
- [7] Y. Xia, D. Qian, D. Hsieh, L. Wray, A. Pal, H. Lin, A. Bansil, D. Grauer, Y. S. Hor, R. J. Cava, and M. Z. Hasan, Nature Phys. **5**, 398 (2009).

- [8] A. Shitade, H. Katsura, J. Kuneš, X.-L. Qi, S.-C. Zhang, and N. Nagaosa, Phys. Rev. Lett. **102**, 256403 (2009).
- [9] D. Pesin and L. Balents, Nature Phys. **6**, 376 (2010).
- [10] J. Chaloupka, G. Jackeli, and G. Khaliullin, Phys. Rev. Lett. **105**, 027204 (2010).
- [11] S. Raghu, X.-L. Qi, C. Honerkamp, and S.-C. Zhang, Phys. Rev. Lett. **100**, 156401 (2008).
- [12] Y. Zhang, Y. Ran, and A. Vishwanath, Phys. Rev. B **79**, 245331 (2009).
- [13] S. Rachel and K. Le Hur, Phys. Rev. B **82**, 075106 (2010).
- [14] D. Zheng, G.-M. Zhang, and C. Wu, Phys. Rev. B **84**, 205121 (2011).
- [15] J. Wen, M. Kargarian, A. Vaezi, and G. A. Fiete, Phys. Rev. B **84**, 235149 (2011).
- [16] T. Yoshida, R. Peters, S. Fujimoto, and N. Kawakami, Phys. Rev. B **87**, 085134 (2013).
- [17] S. Miyakoshi and Y. Ohta, Phys. Rev. B **87**, 195133 (2013).
- [18] J. C. Budich, B. Trauzettel, and G. Sangiovanni, Phys. Rev. B **87**, 235104 (2013).
- [19] M. Dzero, K. Sun, V. Galitski, and P. Coleman, Phys. Rev. Lett. **104**, 106408 (2010).
- [20] J. Werner and F. F. Assaad, Phys. Rev. B **88**, 035113 (2013).
- [21] X. Deng, K. Haule, and G. Kotliar, Phys. Rev. Lett. **111**, 176404 (2013).
- [22] D. Xiao, W. Zhu, Y. Ran, N. Nagaosa, and S. Okamoto, Nat. Commun. **2**, 596 (2011).
- [23] M. Imada, A. Fujimori, and Y. Tokura, Rev. Mod. Phys. **70**, 1039 (1998).
- [24] B. J. Kim, H. Ohsumi, T. Komesu, S. Sakai, T. Morita, H. Takagi, T. Arima, Science **323**, 1329 (2009).



- [25] H. Y. Hwang, Y. Iwasa, M. Kawasaki, B. Keimer, N. Nagaosa, and Y. Tokura, *Nat. Mater.* **11**, 103 (2012).
- [26] X.-L. Qi, T. L. Hughes, and S.-C. Zhang, *Phys. Rev. B* **78**, 195424 (2008).
- [27] L. Fu and C. L. Kane, *Phys. Rev. Lett.* **100**, 096407 (2008).
- [28] J. L. Lado, V. Pardo, and D. Baldomir, *Phys. Rev. B* **88**, 155119 (2013).
- [29] A. Rüegg and G. A. Fiete, *Phys. Rev. B* **84**, 201103(R) (2011).
- [30] K.-Y. Yang, W. Zhu, D. Xiao, S. Okamoto, Z. Wang, and Y. Ran, *Phys. Rev. B* **84**, 201104(R) (2011).
- [31] A. Rüegg, C. Mitra, A. A. Demkov, and G. A. Fiete, *Phys. Rev. B* **85**, 245131 (2012).
- [32] S. Okamoto, *Phys. Rev. Lett.* **110**, 066403 (2013).
- [33] A. Rüegg, C. Mitra, A. A. Demkov, and G. A. Fiete, *Phys. Rev. B* **88**, 115146 (2013).
- [34] D. Doennig, W. E. Pickett, and R. Pentcheva, *Phys. Rev. Lett.* **111**, 126804 (2013).
- [35] D. Doennig, W. E. Pickett, and R. Pentcheva, *Phys. Rev. B* **89**, 121110(R) (2014).
- [36] A. Georges, G. Kotliar, W. Krauth, and M. J. Rozenberg, *Rev. Mod. Phys.* **68**, 13 (1996).
- [37] A. A. Mostofi, J. R. Yates, Y.-S. Lee, I. Souza, D. Vanderbilt, and N. Marzari, *Comput. Phys. Commun.* **178**, 685 (2008).
- [38] G. Kresse and J. Furthmüller, *Phys. Rev. B* **54**, 11169 (1996).
- [39] G. Kresse and D. Joubert, *Phys. Rev. B* **59**, 1758 (1999).
- [40] J. P. Perdew, K. Burke, and M. Ernzerhof, *Phys. Rev. Lett.* **77**, 3865 (1996).
- [41] M. Caffarel and W. Krauth, *Phys. Rev. Lett.* **72**, 1545 (1994).
- [42] C. A. Perroni, H. Ishida, and A. Liebsch, *Phys. Rev. B* **75**, 045125 (2007).
- [43] R. B. Lehoucq, D. C. Sorensen, and C. Yang, *ARPACK Users Guide* (SIAM, Philadelphia, 1997).
- [44] We have checked that bath Green's functions from lattice problems are reproduced by impurity models well. For the discussion on the bath size in ED DMFT, see A. Liebsch and H. Ishida, *J. Phys.: Condens. Matter* **24**, 053201 (2012). For  $t_{2g}$  systems, the low-energy properties are shown to depend weakly on the number of bath levels. Comparison between ED and quantum Monte-Carlo impurity solvers are also presented, showing good agreement.
- [45] M. Capone, M. Civelli, S. S. Kancharla, C. Castellani, and G. Kotliar, *Phys. Rev. B* **69**, 195105 (2004).
- [46] O. Sakai, Y. Shimizu, and T. Kasuya, *J. Phys. Soc. Jpn.* **58**, 3666 (1989).
- [47] S. Okamoto, *Phys. Rev. B* **84**, 201305(R) (2011).
- [48] R. Arita, J. Kuneš, A. V. Kozhevnikov, A. G. Eguiluz, and M. Imada, *Phys. Rev. Lett.* **108**, 086403 (2012).
- [49] R. S. K. Mong, A. M. Essin, and J. E. Moore, *Phys. Rev. B* **81**, 245209 (2010).
- [50] F. Aryasetiawan, M. Imada, A. Georges, G. Kotliar, S. Biermann, and A. I. Lichtenstein, *Phys. Rev. B* **70**, 195104 (2004).
- [51] A. Kozhevnikov, A. Eguiluz, and T. Schulthess, SC'10 Proceedings of the 2010 ACM/IEEE International Conference for High Performance Computing, Networking, Storage, and Analysis (IEEE Computer Society, Washington, DC, 2010), pp. 1-10 (2010).
- [52] For 3d TMOs, LDA+DMFT with Coulomb interactions by cRPA tends to underestimate the mass enhancement [53] because the LDA bare band is wide. This issue is resolved in  $GW$ +DMFT due to the additional band renormalization introduced by  $GW$  [54]. As our systems are 5d TMOs, the Wannier functions are more extended and such effects are expected to be small.
- [53] R. Sakuma, Ph. Werner, and F. Aryasetiawan, *Phys. Rev. B* **88**, 235110 (2013).
- [54] C. Taranto, M. Kaltak, N. Parragh, G. Sangiovanni, G. Kresse, A. Toschi, and K. Held, *Phys. Rev. B* **88**, 165119 (2013).
- [55] H. Zhang, K. Haule, and D. Vanderbilt, *Phys. Rev. Lett.* **111**, 246402 (2013).
- [56] F. Wang and T. Senthil, *Phys. Rev. Lett.* **106**, 136402 (2011).
- [57] S. Wolgast, Ç. Kurdak, K. Sun, J. W. Allen, D.-J. Kim, and Z. Fisk, *Phys. Rev. B* **88**, 180405(R) (2013).
- [58] D. J. Kim, S. Thomas, T. Grant, J. Botimer, Z. Fisk, and J. Xia, *Sci. Rep.* **3**, 3150 (2013).
- [59] X. Zhang, N. P. Butch, P. Syers, S. Ziemak, R. L. Greene, and J. Paglione, *Phys. Rev. X* **3**, 011011 (2013).
- [60] S. Sugano, Y. Tanabe, and H. Kamimura, *Multiplets of Transition-Metal Ions in Crystals* (Academic, New York, 1970).